An experimentally informed grain boundary model in 2–D: addressing triple junctions and invariance of misorientation

S.Syed Ansari[a], Amit Acharya[b], Rajat Arora[c], Alankar Alankar[a,*]

[a] *Department of Mechanical Engineering, Indian Institute of Technology Bombay, Powai, Mumbai–400076, India*

[b] *Department of Civil & Environmental Engineering, and Center for Nonlinear Analysis, Carnegie Mellon University, Pittsburgh, PA 15213, USA*

[c] *Advanced Micro Devices, Inc. (AMD), 7171 Southwest Pkwy, Austin, TX 78735, USA*

Abstract

A novel 2-D continuum model for grain boundaries is presented, incorporating experimentally obtained data on grain boundary energy variation with misorientation. The model is employed to simulate the idealized evolution of grain boundaries within a 2-D grain array, following the methodology outlined in a previous study by us [1]. The approach of the model involves representing misorientation in a continuum scale through spatial gradients of orientation, considered a fundamental field. Based on experimental findings, the dependence of grain boundary energy density on the orientation gradient is found to be generically non-convex. The model employs gradient descent dynamics for the energy to simulate idealized microstructure evolution, necessitating the energy density to be regularized with a higher-order term to ensure the model's well-posedness. From a mathematical perspective, the formulated energy functional fits the Aviles-Giga (AG)/Cross-Newell (CN) category, albeit with non-uniform well depths, leading to unique structural characteristics in solutions linked to grain boundaries in equilibria. The presented results showcase microstructure evolution, and grain boundary equilibria, illustrating reorientation of grains in two dimensional space. Idealized features such as equilibrium high–angle grain boundaries (HAGBs), curvature-driven grain boundary motion, grain rotation, grain growth, and triple junctions that satisfy the Herring condition in our 2-D simulations are also demonstrated.

Keywords: Microstructure evolution, Grain rotation, Grain boundaries, Coarsening.

1. Introduction

The microstructure of polycrystalline materials significantly influences their bulk properties [2]. A comprehensive understanding of grain boundaries (GBs) is crucial for assessing the

*Corresponding author, Tel.: +91-9769415356, Fax: +91-22-25726875

Email addresses: syed.ansari@iitb.ac.in (S.Syed Ansari), acharyaamit@cmu.edu (Amit Acharya), rajat.arora9464@gmail.com (Rajat Arora), alankar.alankar@iitb.ac.in (Alankar Alankar)

overall microstructural evolution and equilibria of polycrystalline materials [3–12]. Building upon [1], this study develops a 2–D continuum-scale GB model using experimentally measured GB energy data.

A consequence of a fundamental physical principle in solids is that superposed rigid body motions of a body cannot incur an energy cost [13]. Adherence of the constitutive description of a solid to the principle ensures that the particular model represents the physical reality that rigid body rotations are energetically neutral. Consequently, a rotationally invariant energy density is critical for physical viability [1]. In our work, GBs are modeled as narrow transition regions with orientation gradients. Instead of using a nonconvex energy density directly dependent on orientation, this study adopts a framework where the energy density is rotationally invariant and dependent on higher-order orientation gradients. Here, the term 'non-convex energy density' refers to an energy density function (of the magnitude, a scalar, of the orientation gradient field) whose second derivative is negative in specific regions within its domain. This perspective couples GB mechanics with internal stress and applied loads, enabling a simplified yet physically consistent 2–D model using proper orthogonal tensors.

As extensively detailed in [1], the proposed model centers on a GB energy density function (ϕ) derived directly from experimental data of GB energy as a function of misorientation. A parameter, l, with dimensions of length is introduced to represent the GB width over which misorientations at physically observed grain boundaries are typically observed to occur. The model transforms variations in GB energy density with misorientation to a function of orientation gradients ($\Delta\theta = l|\nabla\theta|$), where $|\nabla\theta|$ represents the magnitude of $\nabla\theta$ in two dimensions.

To ensure continuous dependence w.r.t initial conditions in energy-minimizing dynamics, the non-convex energy density is regularized using a second-orientation gradient penalty. This regularization is crucial for addressing the orientation profile with sharp kinks. This approach is motivated by physical reasoning described in Section 4.5 of [1].

Our model exhibits formal similarities with the Aviles–Giga [14] (A–G) and Cross–Newell [15] (C–N) functionals, as discussed in [1]. Notably, a key distinction lies in our model's physical requirement for unequal depths to confer non-vanishing energy content to GBs. In the conventional interpretation of the A–G model, energy density troughs correspond to phases (regions of slope ± 1, i.e., 'grains'), and kinks represent phase or GBs in 1–D and 2–D [16]. In contrast, our model designates the GB simply as a phase, akin to the grains but with different spatial extents.

We note that our proposed model may also serve as a suitable mathematical framework in the elasticity of compatible phase transformations [17], with an important distinction in interpretation. In the theory of compatible phase transformations phases are indicative of constant deformation/displacement gradients and it is these gradients that form the argument of the energy density. In the present model, it is orientation gradients (roughly speaking, a higher order gradient of deformation) that incur an energy cost through the energy density employed. Consequently, in the elasticity of compatible phase transformations, work-conjugate quantities involve stresses and forces, while in our case, they manifest as couple-stresses and moments.

Kobayashi, Warren, and Carter (KWC) formulated a continuum grain boundary model

in 2–D employing variables such as the degree of crystallinity (η) and the orientation gradient ($\nabla\theta$) to simulate grain growth through curvature-driven grain shrinkage and rotation mechanisms [3]. This model was later expanded to three dimensions (3-D), where the GB energy is characterized in a five-dimensional misorientation and inclination space [18].

A brief comparison of our work with earlier established contiributions in the literature is as follows. The WCK model [19], while intuitive for representing a wide range of GB energies, was disfavored by the same authors on the basis of the requirement that their model needed to predict localized transition layers as global energy minimizers. Later KWC and KWCL models [3, 20] addressed some of these issues by recovering single transition layer solutions as global minima, which did not allow the use of nonconvex energy densities. Our previous work [1] introduced an experimentally-informed framework that allows persistent local minima solutions under perturbations and exhibits high metastability, providing a robust physical interpretation of GBs as local equilibria. For more details, refer to [1].

The structure of the paper is as follows: Section 1.1 provides a concise literature review. The mathematical formulation of the model is then discussed in Section 2. Subsequently, Section 3 delves into the numerical implementation of the model. Section 4 presents simulations covering microstructure evolution, encompassing grain rotation, curvature-driven GB motion, grain growth, and equilibrium of high-angle grain boundaries (HAGBs) in bi-crystals and tri-crystals with a triple junction in two dimensions (2-D). Section 5 offers concluding remarks.

1.1. Overview of pertinent literature

Phase-field models have been found instrumental in simulating microstructural evolution [21–24], with a comprehensive review available in [25]. Grain growth is often simulated using Allen-Cahn (A–C) equations [26], incorporating a non-convex energy density function and a non-conserved order parameter [27–30]. However, A–C equations fail to represent grain rotation and violate rotational invariance [3].

Ta'asan and co–workers [31] employ a variational approach to compute curvature-driven grain growth, utilizing Mullins' model [32]. In this framework, the GB energy density is a function of the GB plane normal, and the Herring condition [33, 34] is imposed at triple junctions. Esedoglu and colleagues [35] simulate grain growth in large systems through mean curvature-driven motion while ensuring satisfaction of the Herring condition at triple junctions. Their approach involves the use of the linear diffusion equation along with signed distance functions [36]. Additionally, Bulatov and co–workers propose a level-set method for simulating anisotropic grain growth based on the five-parameter misorientation and inclination GB energy space [37]. Building on this work [37], Nino et al [38] investigate the impact of anisotropy by comparing results in various statistical microstructural descriptors against existing simplified isotropic and anisotropic models.

Glasner conducted computational studies on the gradient flow dynamics of the A-G functional [16] and subsequently formulated a model based on matched asymptotic expansion. This model describes the evolution of GBs and junctions pertinent to the singular limit of the gradient flow associated with the A-G functional. In this model, GB motion is attributed to interface curvature and variations in "line energy" along GBs. Notably, Glasner speculates,

based on numerical simulations, about the potential termination of GBs in bulk, suggesting the presence of disclinations.

A crystal plasticity model, in conjunction with the continuum phase-field model (KWC), is utilized to comprehensively simulate GB sliding, shear-induced GB motion, GB rotation, and curvature-driven grain shrinkage [39]. In the study of polycrystals, Basak and Gupta's significant 2-D [40] and 3-D [41] models effectively address diffusion-controlled incoherent interfaces involving junctions. Characterized as a *sharp interface model*, their framework incorporates curvature-dependent GB energy and surface diffusion, drawing inspiration from the work of Gurtin et al. [42].

Efforts to link GB evolution with geometric parameters continue. Rollett et al. [43] found correlations between GB mobility and five-parameter GB distributions, while Zhang et al. [29] and Aditi et al. [44] reported varying correlations with GB curvature and velocity. These studies highlight the need for a model that mechanistically describes GB evolution using experimental data.

As an alternative approach to curvature-driven models, Srolovitz et al. have introduced a continuum equation of motion for GBs and constructed models based on the discrete disconnection mechanism, as demonstrated in their recent works [6, 45, 46]. Furthermore, they extended this framework to encompass polycrystals [4], investigating the impact of anisotropy in both kinetic and thermodynamic properties [47].

Our study in [1] introduces a novel approach by employing a rotationally invariant (or frame-indifferent) energy density in a phase-field-like model, utilizing atomistically determined or experimentally measured GB energies. To the best of our knowledge, no phase–field model has been reported addressing frame indifference / rotational invariance along with experimentally measured GB energy density for simulating the dynamics of various GBs in two-dimensional space. The experimentally measured GB energy density indicates the presence of equilibrium High-Angle Grain Boundaries (HAGBs) [48], a feature not accounted for in existing phase-field-based GB models [1]. Given these considerations, the principal objectives of the current study are to extend our established 1-D model [1] into the 2-D realm, encompassing the following key features:

- Implementation of an experimentally measured grain boundary (GB) energy function to drive the evolution of GBs in 2-D.
- Addressing rotational invariance within the model.
- Capturing equilibrium transition layers in two–dimensional grain array, serving as an idealized representation of equilibrium HAGBs.
- Demonstrating aspects of idealized grain rotation, curvature-driven GB motion, and grain growth in 2-D.
- Achieving local equilibrium at the triple junction by satisfying the Herring condition.

The model proposed in this study can effectively capture equilibrium transition layers within a 2-dimensional grain array as an idealized representation of equilibrium HAGBs. Our model

shows grain growth through grain reorientation and curvature-driven GB motion, idealized in two spatial dimensions.

Complementing [31], this work treats GBs and triple junctions as localized features within a continuous orientation field, diverging from discrete object approaches. By addressing experimentally measured GB energy density and rotational invariance, our model offers a robust framework for simulating GB evolution using experimental data. Further details can be found in [1].

2. Mathematical formulation of the 2-D Continuum Grain Boundary Model

In this work, we restrict attention to 2–D where one angle parameter (orientation (θ)) suffices. The variable (θ) is defined as the angle in radians between the crystal frame x-axis (X_P/X_N) and the reference frame x-axis (X_R). Here, (X_P) denotes the crystal frame making a positive rotation angle (θ_P) with (X_R), while (X_N) denotes the crystal frame making a negative rotation angle (θ_P) with (X_R) as illustrated in Fig. 1. We consider the spatial domain $\Omega = (0, L_1) \times (0, L_2)$. Time is represented by the letter t. The free energy of the system(F), a fundamental concept in our study, is formulated as

$$F = \int_\Omega \varphi\left(\nabla\theta, \mathcal{L}\theta, l\right)\, d\Omega, \tag{1}$$

where $\mathcal{L}$(Laplacian) $= div\ grad$, $\varphi\left(\nabla\theta, \mathcal{L}\theta, l\right)$ is the overall free energy density, formulated as follows:

$$\varphi\left(\nabla\theta, \mathcal{L}\theta, l\right) = \phi\left(\nabla\theta\right) + \epsilon^2\left(\mathcal{L}\theta\right)^2.$$

The parameter l is a significant factor, representing a characteristic GB width. This parameter is pivotal in defining the function ϕ and understanding the system's behavior. Additionally, we have the material parameter ϵ, which is introduced based on dimensional considerations. This parameter serves as a representation of the energetic penalty associated with the presence of sharp kinks in the orientation profile [1].

The gradient flow evolution of the functional F is described by

$$\partial_t\theta = -M\frac{\delta F}{\delta\theta}, \tag{2}$$

where M represents a scalar mobility factor that scales the variational derivative of functional F. The variation of F in the η direction about the state θ is described as

$$\begin{aligned}\delta F = \int_\Omega \left[\partial_j\partial_j\left(\frac{\partial\varphi}{\partial\left(\mathcal{L}\theta\right)}\right) - \partial_i\left(\frac{\partial\varphi}{\partial\left(\nabla\theta\right)}\right)_i\right]\eta\, d\Omega \\ + \int_{\partial\Omega}\eta\left(\left[\left(\frac{\partial\varphi}{\partial\left(\nabla\theta\right)}\right)_j - \partial_j\left(\frac{\partial\varphi}{\partial\left(\mathcal{L}\theta\right)}\right)\right]n_j\right)dS \\ + \int_{\partial\Omega} n_j\partial_j\eta\left(\left[\frac{\partial\varphi}{\partial\left(\mathcal{L}\theta\right)}\right]\right)dS,\end{aligned} \tag{3}$$

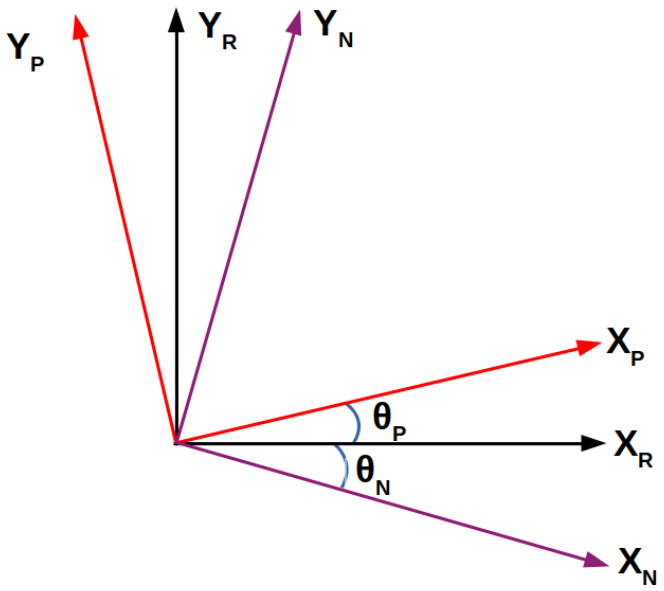

Figure 1: Representation of orientation (θ) with respect to the reference frame (X_R). Here, (X_P) denotes the crystal frame making a positive rotation angle (θ_P) with (X_R), while (X_N) denotes the crystal frame making a negative rotation angle (θ_N) with (X_R).

where n_j represents j^{th} component of the unit normal vector. The variational derivative is then described as

$$\frac{\delta F}{\delta \theta} = \partial_l \partial_l \left(\frac{\partial \varphi}{\partial \left(\mathcal{L}\theta \right)} \right) - \partial_j \left(\frac{\partial \varphi}{\partial \left(\nabla \theta \right)} \right)_j . \tag{4}$$

Among the potential boundary conditions stemming from Eq. (3) are

$$\theta = \text{specified}; \qquad \nabla\theta \cdot \hat{n} = \text{specified}; \tag{5a}$$

$$\theta = \text{specified}; \qquad \frac{\partial \varphi}{\partial \left(\mathcal{L}\theta \right)} = \text{specified}; \tag{5b}$$

$$\left(\frac{\partial \varphi}{\partial \left(\nabla \theta \right)} - \nabla \left(\frac{\partial \varphi}{\partial \left(\mathcal{L}\theta \right)} \right) \right) \cdot \hat{n} = \text{specified}; \qquad \frac{\partial \varphi}{\partial \left(\mathcal{L}\theta \right)} = \text{specified}; \tag{5c}$$

$$\nabla\theta \cdot \hat{n} = \text{specified}; \qquad \left(\frac{\partial \varphi}{\partial \left(\nabla \theta \right)} - \nabla \left(\frac{\partial \varphi}{\partial \left(\mathcal{L}\theta \right)} \right) \right) \cdot \hat{n} = \text{specified}; \tag{5d}$$

(other possibilities, involving combinations of these conditions on mutually exclusive parts of the boundary exist). Substituting Eq. (4) into Eq. (2), one obtains

$$\partial_t \theta = -M \left(\partial_l \partial_l \left(\frac{\partial \varphi}{\partial \left(\mathcal{L}\theta \right)} \right) - \partial_i J_i \right), \tag{6}$$

where $J = \frac{\partial \varphi}{\partial (\nabla \theta)}$, as the governing equation. In this work we use the boundary condition

Eq. (5d), specified to vanish:

$$\begin{aligned} \partial_k \theta n_k &= 0, \\ \left(J_k - \partial_k \left(\frac{\partial \varphi}{\partial \left(\mathcal{L}\theta \right)} \right) \right) n_k &= 0. \end{aligned} \tag{7}$$

This boundary condition is chosen here, but any of the other combinations in Eq. (5) could also be utilized. We use it for simplicity, noting that it is not a central focus of this work.

2.1. Experimental data based grain boundary (GB) energy density functions

The determination of GB energy concerning misorientation is a well-established practice, with documented measurements available in the literature [48–50]. Read and Shockley's groundbreaking work [51] theoretically derived a density function for GB energy, rooted in dislocation mechanics principles, applicable within the context of small misorientations, and aligning with an energy density cusp at 0 misorientation. The application of the variational method to compute interfacial energies of tilt boundaries has revealed cusps in the ϕ function [48]. For FCC metals, a GB energy function characterized by these cusps has been proposed, relying on the fundamental five macroscopic degrees of freedom [52]. However, examining the GB energy density (ϕ) in copper using molecular dynamics (MD) simulations reveals a notably smoother ϕ function [53]. The literature reports various forms of ϕ, and there is no definitive consensus on its exact shape [1].

The evolution equation (Eq. (6)) operates on a dimensional grain boundary energy density function, typically derived from experimentally measured data [48]. This data, covering misorientations ($\Delta\theta$), is transformed into a function of $|\nabla\theta|$, as described in Section 1. Extending this function as an even function over a defined range characterizes the change in the fundamental period of a periodic function ϕ across the real line, essential for our calculations [1].

Hasson and Goux's experimental data [48] is correlated with two distinct ϕ functions in [1]: one is a smooth energy density (SED) denoted ϕ_s, and the other is a cusp energy density (CED) denoted ϕ_c.

The SED function, derived from a cubic spline interpolation of the complete experimental dataset, closely represents all energy troughs observed in the experimental data, presumed to be the closer reality in this context. This includes even the higher energy troughs. In contrast, the CED function is generated by fitting chosen experimental data points with piecewise–non–convex quadratic segments. These segments are linked together through smooth transitions positioned around the local minima of the energy density data. Notably, both functions exhibit non-convex characteristics, with troughs of varying depths. In this study, we opted to utilize the SED (ϕ_s) since it captures all the troughs in the experimental data and is assumed to be the ground truth.

As discussed in [1], the evolution Eq. (6) utilizes a dimensional SED (ϕ_s) function fitted to experimentally measured GB energy density data in [48].

The energy density function ϕ_s is discretized into N segments according to the methodology outlined in [1]. Within this discretization, the value of ϕ at a specific point, $|\nabla\theta|$, can be obtained as

$$\phi(|\nabla\theta|) = \mathcal{R}_q(|\nabla\theta|), \qquad |\nabla\theta|_q^s \leq |\nabla\theta| \leq |\nabla\theta|_q^f,$$

where, each $\mathcal{R}_q(|\nabla\theta|)$ represents the q^{th} segment of the $\phi(|\nabla\theta|)$ function. The values $|\nabla\theta|_q^s$ and $|\nabla\theta|_q^f$ denote the starting and ending points of this q^{th} segment, respectively. The index q varies from 1 to N.
In accordance with the view presented in [1], the expression for the SED (ϕ_s) function corresponding to the GB energy density data in [48] can be described as

$$\mathcal{R}_q(|\nabla\theta|) = B\left(a_q\left(|\nabla\theta|l\right)^3 + b_q\left(|\nabla\theta|l\right)^2 + c_q|\nabla\theta|l + d_q\right), \qquad |\nabla\theta|_q^s \leq |\nabla\theta| \leq |\nabla\theta|_q^f, \quad (8)$$

where, the parameter B represents a dimensional material constant that scales the data from relative to actual GB energy density, essentially setting the energy scale for the problem. The parameter l denotes the GB width, crucial for converting misorientation ($\Delta\theta$) into orientation gradients. Through non-dimensionalization, this transformation potentially enables the interpretation of orientation gradients as misorientation. The coefficients a_q, b_q, c_q, and d_q define the cubic polynomial specific to the q^{th} segment of the overall spline. These coefficients are carefully chosen to ensure that the overall energy density function maintains continuous differentiability across the fundamental period.

Fig. 2 illustrates the SED function, which is an interpolating function for the experimental data. Additionally, it showcases the first derivative of this function. Notably, the SED function possesses physical dimensions that correspond to energy density. The substitution of the expression from Eq. (8) into the overall free energy equation of the system in Eq. (1) yields the final evolution equation associated with ϕ_s.

The non-dimensional form of the governing equation (Eq. (6)), as a result of non-dimensionalization, is

$$\partial_{\widetilde{t}}\theta = -\alpha\widetilde{\nabla}^4\theta + \widetilde{\nabla}\cdot\widetilde{J}\left(\widetilde{\nabla}\theta\right) \quad (9)$$

where,

$$x_i = l\widetilde{x_i}, \qquad t = \frac{l\widetilde{t}}{MB}, \qquad \nabla\theta = \frac{1}{l}\frac{\partial\theta}{\partial\widetilde{x_i}} = \frac{1}{l}\widetilde{\nabla}\theta, \qquad \partial_t\theta = \frac{MB\partial_{\widetilde{t}}\theta}{l}, \qquad \alpha = \frac{2\epsilon^2}{Bl^3}.$$

In this context, it's important to remember that the variable l corresponds to the width of the GB, while M signifies the GB mobility. Additionally, ϵ quantifies the energy penalty associated with the presence of sharp kinks in the orientation profile. The notation $\widetilde{\ }$ placed above a variable signifies that it has been non-dimensionalized to remove its original dimensions.

From this point forward, we will exclusively focus on the non-dimensionalized problem. To simplify notation for clarity, we will no longer include the overhead $\widetilde{\ }$ on variables.

[*] $\nabla\cdot J = divJ$

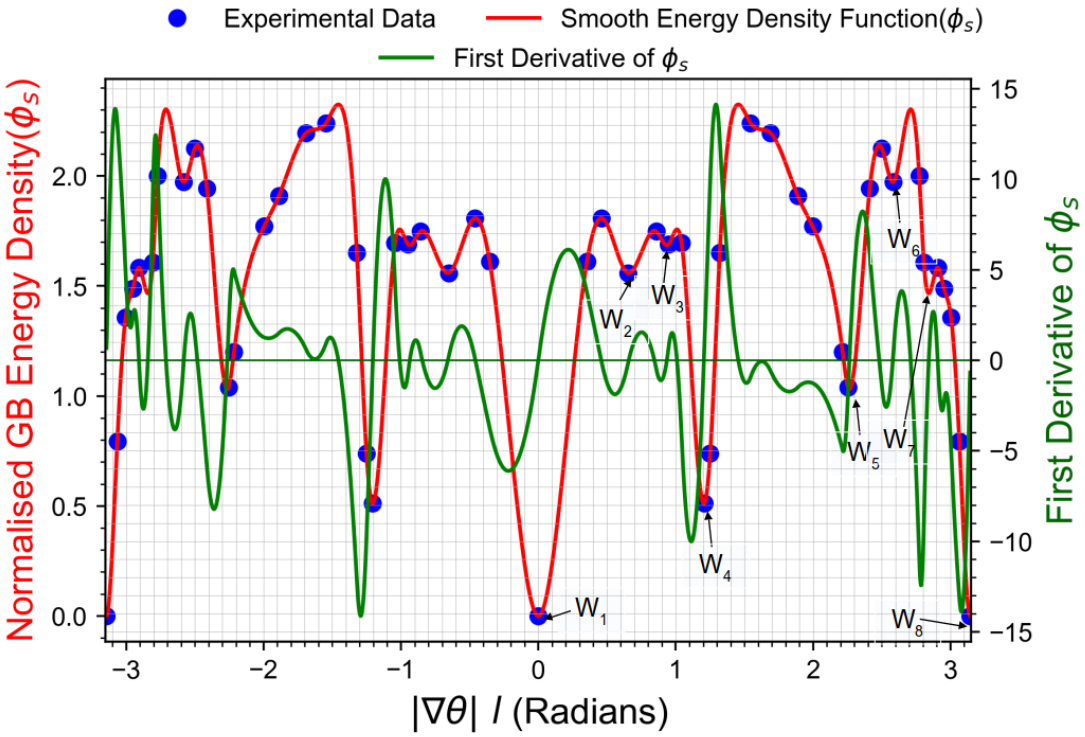

Figure 2: Fitting a smooth curve to represent grain boundary energy density as a function of $|\nabla\theta|$ based on experimental data obtained from [48]. $W_1, W_2, ...W_8$ denote the different wells in the SED function, while l represents the width of the grain boundary [1].

3. Numerical Implementation

The governing equation of the present model (Eq. (9)) is fourth–order in space. A mixed formulation approach is followed. The fourth–order equation is split into two-second–order equations as follows:

$$\partial_t\theta = -\alpha\partial_l\partial_l v + \partial_k J_k, \tag{10a}$$

$$v - \partial_i\partial_i\theta = 0. \tag{10b}$$

The test functions w and q are multiplied with Eq. (10) and integrate as

$$\int_\Omega w\partial_t\theta d\Omega = -\int_\Omega w\alpha\partial_j\partial_j v d\Omega + \int_\Omega w\partial_i J_i d\Omega, \tag{11a}$$

$$\int_\Omega qv d\Omega - \int_\Omega q\partial_l\partial_l\theta d\Omega = 0. \tag{11b}$$

The corresponding weak form for the Eq. (10) is

$$\int_\Omega w\partial_t\theta d\Omega = \int_\Omega \alpha\partial_j w\partial_j v d\Omega - \int_\Omega \partial_i w J_i d\Omega + \int_{\partial\Omega} w\left(J_k - \alpha\partial_k v\right) n_k dS; \tag{12a}$$

$$\int_\Omega qv d\Omega + \int_\Omega \partial_l q\partial_l\theta d\Omega - \int_{\partial\Omega} q\partial_k\theta n_k dS = 0. \tag{12b}$$

The boundary terms in Eq. (12) are set to zero and the boundary conditions chosen for the present work are

$$\partial_k\theta n_k = 0, \tag{13a}$$

$$(J_k - \alpha\partial_k v)n_k = 0. \tag{13b}$$

The spatial discretization is carried out as

$$\theta_h(x,t) = \sum_{i=1}^{N}\Theta_j(t)N_j(x) \quad \& \quad v_h(x,t) = \sum_{i=1}^{N} V_j(t)N_j(x),$$

where $V_j(t)$ and $\Theta_j(t)$ are scalars. The test functions w and q are replaced by N_i and the Eq. (12) becomes

$$\partial_t\Theta_j(t)\int_\Omega N_i N_j d\Omega = \alpha V_j\int_\Omega \nabla N_i\cdot\nabla N_j d\Omega - \int_\Omega \nabla N_i\cdot J d\Omega; \tag{14a}$$

$$V_j\int_\Omega N_i N_j d\Omega + \Theta_j\int_\Omega \nabla N_i\cdot\nabla N_j d\Omega = 0. \tag{14b}$$

The Euler forward method is used to discretize in time, and the Eq. (14) becomes

$$M\Theta_j^n = \alpha V_j^{n-1}Adt + M\Theta_j^{n-1} - F^{n-1}dt; \tag{15a}$$

$$MV_j^{n-1} = -A\Theta_j^{n-1}. \tag{15b}$$

where,

$$M_{ij} = \int_\Omega N_i N_j d\Omega,\ A_{ij} = \int_\Omega \nabla N_i\cdot\nabla N_j d\Omega, \quad \& \quad F_i = \int_\Omega \nabla N_i\cdot J d\Omega$$

where M is the mass matrix, A is the stiffness matrix, and the superscripts n and $n-1$ over a variable represent the variable calculated at current and previous time steps respectively.

The final formulation in Eq. (15) requires C^0 continuity at the junctions of the finite elements. Therefore, it could be solved using the Lagrange elements in the deal.II [54], the open-source finite element library in which the framework has been implemented. We first solve for V_j^{n-1} in Eq. (15b) and substitute it in Eq. (15a) and solve for Θ_j^n. Repeat this process by increment in time until the system attains equilibrium.

Let us consider Eq. (8) for evaluation of the energy density

$$\phi(|\nabla\theta|) = \Re_q(|\nabla\theta|) = B\left(a_q|\nabla\theta|^3 + b_q|\nabla\theta|^2 + c_q|\nabla\theta| + d_q\right), \qquad |\nabla\theta|_q^s \le |\nabla\theta| \le |\nabla\theta|_q^f.$$

Now evaluate $J(\nabla\theta) = (\frac{\partial\phi}{\partial(\nabla\theta)})$ as

$$J(\nabla\theta) = B\left(3a_q|\nabla\theta|^2\frac{\nabla\theta}{|\nabla\theta|} + 2b_q|\nabla\theta|\frac{\nabla\theta}{|\nabla\theta|} + c_q\frac{\nabla\theta}{|\nabla\theta|}\right), \qquad |\nabla\theta|_q^s \le |\nabla\theta| \le |\nabla\theta|_q^f, \quad (16)$$

Note that $\frac{\partial|\nabla\theta|}{\partial\nabla\theta} = \frac{\nabla\theta}{|\nabla\theta|}$ where $|\nabla\theta| = \sqrt{\nabla\theta\cdot\nabla\theta}$. Additionally, $J_2(|\nabla\theta|) := \frac{\partial^2\phi}{\partial|\nabla\theta|^2}$ is only used for the calculation of the stable time step in Eq. (21) as detailed in [1], and it can be computed as

$$J_2(|\nabla\theta|) = B\left(6a_q|\nabla\theta| + 2b_q\right), \qquad |\nabla\theta|_q^s \le |\nabla\theta| \le |\nabla\theta|_q^f. \quad (17)$$

The discontinuity in $\frac{\nabla\theta}{|\nabla\theta|}$ at $\nabla\theta = 0$ in Eq. (16) is smoothed by the use of $\frac{\tanh(\gamma|\nabla\theta|)}{|\nabla\theta|}\nabla\theta$ [55] based on which J is rewritten as

$$J(\nabla\theta) = B\left(3a_q|\nabla\theta|^2 + 2b_q|\nabla\theta| + c_q\right)\tanh(\gamma|\nabla\theta|)\frac{\nabla\theta}{|\nabla\theta|}, \quad (18)$$

where the $\gamma = 100$ is used for all the simulations.

3.1. Von Neumann stability analysis

Von Neumann stability analysis offers the time-stepping constraints applicable to discretized linear partial differential equations with constant coefficients. This analysis is particularly relevant for various numerical methods, including finite difference schemes [56]. The term represented by J in Eq. (9) exhibits strong nonlinearity. In accordance with the methodology outlined in [1], we express our equation in the following 1–D as

$$\partial_t\theta = -\alpha\partial_x^4\theta + J_2\left(\partial_x\theta\right)\partial_x^2\theta, \quad (19)$$

assume J_2 as a constant coefficient, conduct a Von Neumann stability analysis, extract the time step constraint(s) associated with the J_2 value at each node, and ultimately select the minimum of these constraints across the entire domain. The growth factor corresponding to the explicit scheme is acquired from the expression

$$\theta_k^{t+dt} = \left(1 - \frac{\alpha(2\cos(2k\Delta x) - 8\cos(k\Delta x) + 6)dt}{(\Delta x)^4} + \frac{J_2(2\cos(k\Delta x) - 2)dt}{(\Delta x)^2}\right)\theta_k^t.$$

This leads to the following stability constraint:

$$\left|1-\frac{\alpha(2\cos(2k\Delta x)-8\cos(k\Delta x)+6)dt}{(\Delta x)^4}+\frac{J_2(2\cos(k\Delta x)-2)dt}{(\Delta x)^2}\right|\leq 1+\mathcal{O}(dt)\quad \forall\, 0\leq k\leq\infty \tag{20}$$

(well-posed growth of the solution has to be allowed for $J_2<0, \alpha>0$) where,

$$0\leq(2\cos(2k\Delta x)-8\cos(k\Delta x)+6)\leq 16;\qquad -4\leq(2\cos(k\Delta x)-2)\leq 0.$$

The stability constraints for the scheme are as follows ($\Delta x>0$):

$$dt\leq\begin{cases}\frac{\Delta x^2}{2J_2}, & \alpha=0,\ J_2\geq 0\\ \text{No viable time step}, & \alpha=0,\ J_2<0\\ \frac{\Delta x^4}{8\alpha}, & \alpha>0,\ J_2=0\\ \frac{\Delta x^4}{8\alpha}, & \alpha>0,\ 0<\Delta x\leq\sqrt{\frac{4\alpha}{|J_2|}},\ J_2<0\\ \frac{\Delta x^4}{2(4\alpha+|J_2|\Delta x^2)}, & \alpha>0,\quad J_2\geq 0.\end{cases} \tag{21}$$

As previously mentioned, we calculate the time step (dt) at all nodes based on the stability constraints in Eq. (21). Subsequently, we select the smallest value among all nodes as the stable time step for solving Eq. (15).

4. Results and Discussion

The results detailed in this section are produced utilizing the finite element method (FEM) based formulation presented in Section 3. The adaptive time stepping (dt) expressed in Eq. (21) is multiplied with a factor of 0.02 and a value of 100 is used for γ in Eq. (18) for all simulations. The simulations in this section are performed using the SED (ϕ_s) function in Fig. 2.
In this section, we discuss the following:

- grain rotation;
- equilibrium high–angle grain boundaries (HAGBs) emerging from the sharp boundaries;
- curvature–driven GB motion and grain growth;
- local equilibrium of triple junctions by satisfying Herring condition.

4.1. Bi-crystal with straight grain boundary

Polycrystalline materials typically exhibit GBs between individual grains, which may appear immobile under certain conditions. Experimental observations indicate that GBs in bi-crystal configurations, specifically those without the influence of multi-junction constraints, remain stationary in the absence of external forces such as stress or electromagnetic fields

[57–60]. Furthermore, straight boundaries, as opposed to curved ones, are notably resistant to movement in these circumstances. This case study aims to test the model in producing an idealized equilibrium straight GB between two grains, i.e. a bicrystal. As per the literature, a misorientation angle $\Delta\theta$ less than or equal to 10° is categorized as part of the grain interior (including the sub-grain boundaries), while a misorientation angle greater than 10° is designated as a grain boundary (HAGBs) [61]. To correlate the ranges of misorientation angles ($\Delta\theta$) with $|\nabla\theta|$, as transformed by $\Delta\theta = |\nabla\theta|l$, as discussed in Section 1, and subsequently non-dimensionalized as presented in Eq. (9), the grain interior is now defined as $|\nabla\theta| \leq 0.1745$ (equivalent to $\Delta\theta \leq 10°$), and a GB is defined as $|\nabla\theta| > 0.1745$ (analogous to $\Delta\theta > 10°$) [1].

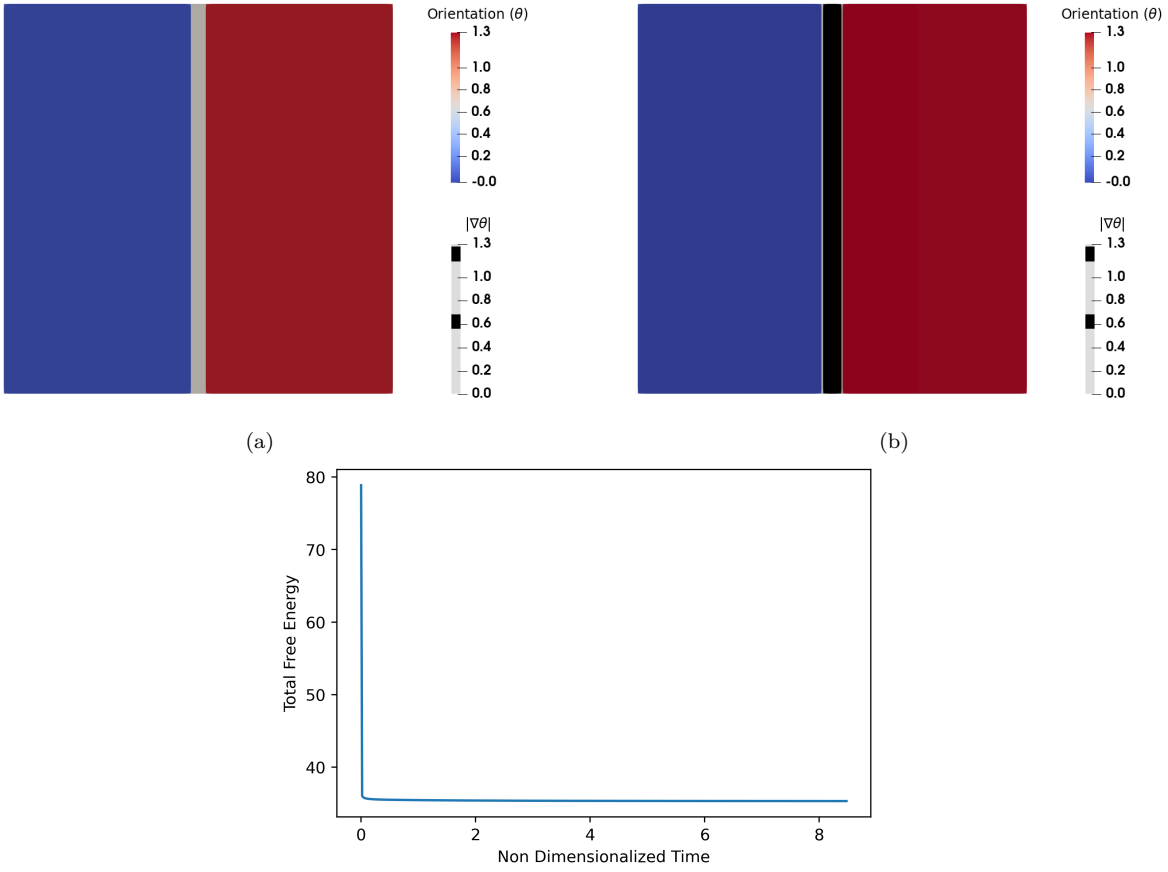

Figure 3: The temporal evolution of orientation in a bi-crystal with straight GB at a time (a) $t = 0$, and (b) $t = 8.48$. The energy density function is SED and $\alpha = 0.07$. The system achieves the final equilibrium profile corresponding to $max_{xx}|(\theta^{t+dt} - \theta^t)/dt| < 1 \times 10^{-3}$. The corresponding total energy evolution over time is depicted in (c). Different colours represent different orientations of the grains, and black colour represents GBs corresponding to energy density wells in Fig. 2.

Fig. 3a depicts the initial state of a bi-crystal featuring a straight, non-equilibrium GB highlighted in grey. In this configuration, the magnitude of the gradient of the orientation

field, $|\nabla\theta|$, is recorded at 1.28, indicating its distance from the local minima of $|\nabla\theta|$ ($|\nabla\theta| \approx 1.2$) as illustrated in Figure 2.

The simulation begins with this initial condition and is allowed to evolve using the SED function until it attains equilibrium, defined by the criterion $max_{xx}|(\theta^{t+dt}|_x - \theta^t|_x)/dt| < 1 \times 10^{-3}$.
Consequently, the simulation results in the emergence of a straight, equilibrium GB depicted in black in Fig. 3b, corresponding to the $|\nabla\theta| = 1.2$ well in Figure 2.

The GB in this equilibrium state adjusts its width to align with the characteristic $|\nabla\theta|$ value of the well, and it remains in this state until the system reaches the aforementioned equilibrium criterion.

These model outcomes are in line with experimental observations, which show that straight GBs remain stationary in the absence of external forces like stress or electromagnetic fields. Furthermore, they demonstrate the capacity of the model to lower the overall energy of the system by naturally producing equilibrium GBs that correspond to the local minima of $|\nabla\theta|$.

4.2. Bi-crystal with circular grain boundary

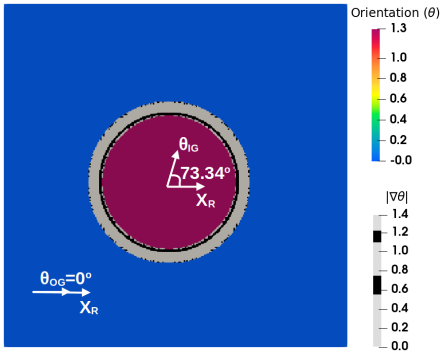

(a) $\theta_{IG} \approx 1.28$ radians/73.34°

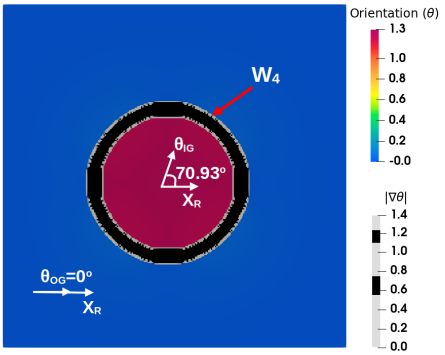

(b) $\theta_{IG} \approx 1.238$ radians/70.93°

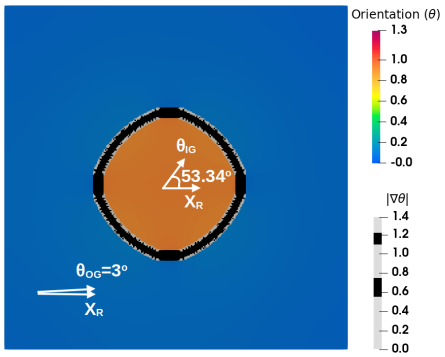

(c) $\theta_{IG} \approx 0.931$ radians/53.34°

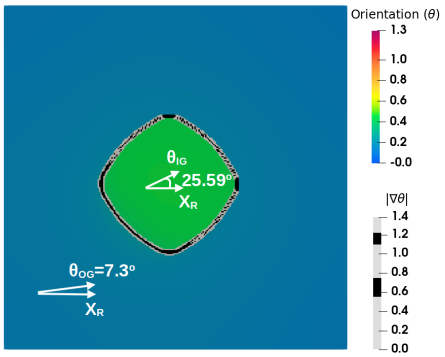

(d) $\theta_{IG} \approx 0.464$ radians/25.59°

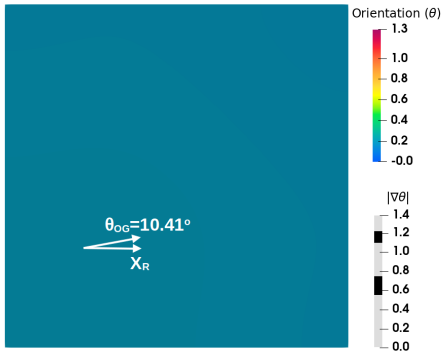

(e)

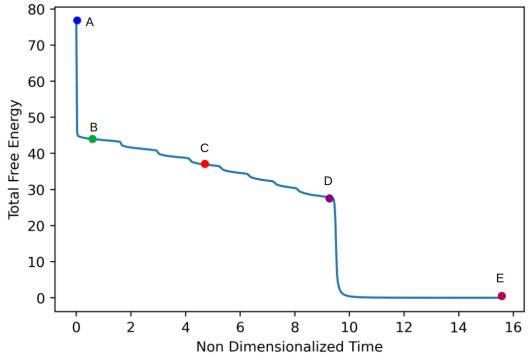

(f)

Figure 4: The temporal evolution of orientation in a bi-crystal with circular grain at a time (a) $t = 0$, (b) $t = 0.48$, (c) $t = 4.91$, (d) $t = 9.45$, and (e) $t = 15.61$. Here, θ_{IG}, θ_{OG}, and X_R denote the orientations of the inner grain, outer grain, and the reference frame, respectively. The energy density function is SED and $\alpha = 0.05$. The system achieves the final equilibrium profile corresponding to $max_{xx}|(\theta^{t+dt} - \theta^t)/dt| < 1 \times 10^{-3}$. The corresponding total energy evolution over time is shown in (f), where points A, B, C, D, and E indicate the total energy of the system at the states depicted in (a), (b), (c), (d), and (e), respectively. Different colors represent different orientations of the grains, and black color represents GBs corresponding to energy density wells in Fig. 2.

Experiments suggest that grain growth can result from the combined effects of curvature-driven GB motion and grain rotation [62, 63]. This proposition finds support in various simulation technique results [3, 64, 65]. In Fig. 4a, a circular grain (red) is initially embedded within a larger grain (blue) with a different orientation. The initial $|\nabla\theta| = 1.28$, represented by the grey region in Fig. 4a, is distant from the equilibrium wells in Fig. 2. As the system evolves over time, the circular grain rotates with respect to the larger blue grain, forming a metastable HAGB corresponding to the $|\nabla\theta| = 1.2$ well in Fig. 2. The change in color represents the orientation change of the circular grain.

Continuing the evolution shown in Fig. 4c and Fig. 4d, the system does not equilibrate with the grain boundary in the $|\nabla\theta| = 1.2$ well. The outer and inner grains gradually rotate toward each others' orientations, as indicated by the changing colors. Despite the persistence of the $|\nabla\theta| = 1.2$ condition, the grain boundary (GB) width reduces (reflecting the metastability of the system), and the GB migrates inward toward the center of the inner grain by a small amount.

Eventually, the inner circular grain disappears, as seen in Fig. 4e, by aligning its orientation with that of the outer grain. This occurs primarily through grain rotation, supplemented by small curvature-driven GB motion (in this case). These results highlight the model's capability to capture grain growth and annihilation driven by grain rotation coupled with curvature-driven GB motion. We suspect that the deviation of the computed evolution from radial symmetry is a combination of the use of a structured square mesh and, possibly, the square shape of the outer domain - a conclusion partially supported by obtaining exactly the same evolution rotated by 45°, in a simulation in which the external square boundary was rotated by the same angle. A detailed computational exploration of such deviations is left for future study, involving a radially symmetric mesh and geometry.

4.3. Tri-crystal with sharp grain boundaries

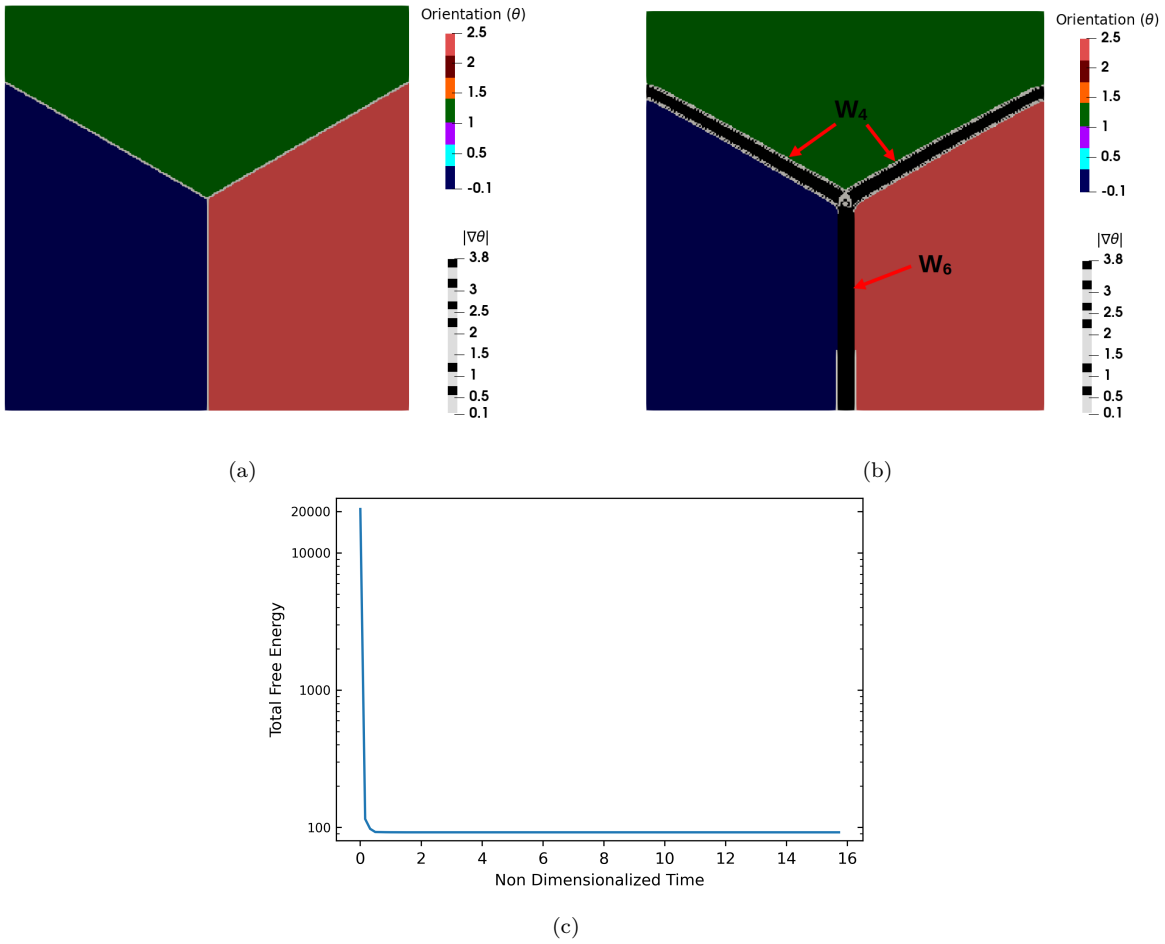

Figure 5: The temporal evolution of orientation ($\theta = 0,\ 1.2,\ \&\ 2.4$) in a tri-crystal with sharp straight GBs initial condition at time (a) $t = 0$, and (b) $t = 15.72$. The energy density function is SED and $\alpha = 0.07$. The system achieves the final equilibrium profile corresponding to $max_{xx}|(\theta^{t+dt} - \theta^t)/dt| < 1 \times 10^{-3}$. The corresponding total energy evolution over time is depicted in (c). Different colours represent different orientations of the grains, and black colour represents GBs corresponding to energy density wells in Fig. 2.

A tri–crystal with sharp non-equilibrium GBs (grey) initial condition is shown in Fig. 5a. The initial orientations of the grains are 0 (blue), 1.2 (green), and 2.4 (red). The current initial condition is allowed to evolve with time. The sharp GBs become widened and produce equilibrium GBs (black) with finite width and a triple junction as shown in Fig. 5b. The vertical equilibrium GB produced in Fig. 5b corresponds to the $|\nabla\theta| = 2.6$ well family in Fig. 2 and the other two are corresponding to the $|\nabla\theta| = 1.2$ well family. Note that some of these GBs belong to distinct wells, each possessing varying GB energies. In experimental observations, it is noticed that the existence of GBs with finite widths and different energies corresponds to the misorientation. It is also worth mentioning that in the Fig. 5b, the triple junction in grey colour signals that it does not align with any of the equilibrium well misorientations. This deviation from the expected alignment could be attributed to energy considerations within the triple junction. From this simulation, it is clear that the model can produce a triple junction and GBs with a finite width corresponding to the equilibrium wells even out of an initial condition with sharp boundaries, which is in line with the experimental findings [61].

Experimental results have unequivocally demonstrated the phenomenon of curvature-driven GB motion. As a natural extension of these findings, the upcoming study aims to replicate the transition from initially curved non-equilibrium GBs to straight GBs driven by curvature within the context of a tricrystal system featuring a triple junction. As initial conditions for this investigation, we utilize a tricrystal system with a distinct set of sharp and curved non-equilibrium GBs, as indicated in Fig. 6a. Notably, the initial grain orientations are designated as follows: 0 (blue), 1.2 (green), and 2.4 (red). This initial condition is then subjected to temporal evolution. In Fig. 6b, the initially sharp GBs undergo a transformation, widening and giving rise to GBs with finite width. However, these new boundaries remain distinct from the equilibrium well, except for the vertical straight GB separating the blue and red grains. Apart from this specific vertical GB, the other two GBs maintain their curvature.

The subsequent stages of GB evolution, as depicted in Fig. 6c and Fig. 6d, reveal that these initially curved GBs eventually transition into straight GBs characterized by $|\nabla\theta|$ values that align with the equilibrium well. This evolution leads to the formation of an equilibrium triple junction characterized by straight GBs. In Fig. 6d, it is noteworthy that the vertical GB belongs to the $|\nabla\theta| = 2.6$ well family, as depicted in Fig. 2, while the other two correspond to the $|\nabla\theta| = 1.2$ well family, mirroring the findings in Fig. 5b. Furthermore, in Fig. 6d, the triple junction in grey colour is a noteworthy observation, as it remains distinct from any of the equilibrium well misorientations. This finding closely parallels the results depicted in Fig. 5b, underscoring the consistent divergence of the triple junction from equilibrium well configurations. This simulation unequivocally demonstrates the model's capacity to generate an equilibrium triple junction and straight GBs with finite widths, even when initiated from the conditions of sharp and curved non-equilibrium boundaries. This outcome serves as compelling evidence that the model successfully replicates the curvature-driven GB motion observed in experimental settings along with the presence of a triple junction.

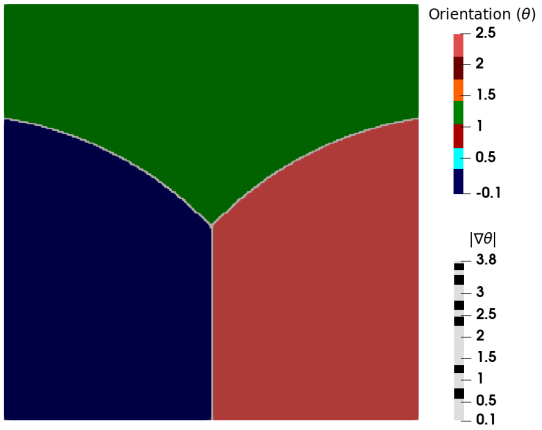

(a)

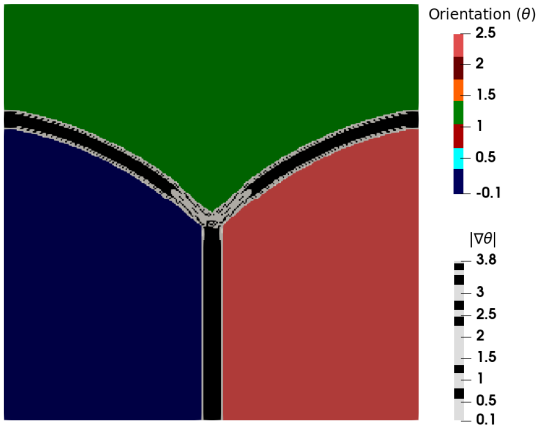

(b)

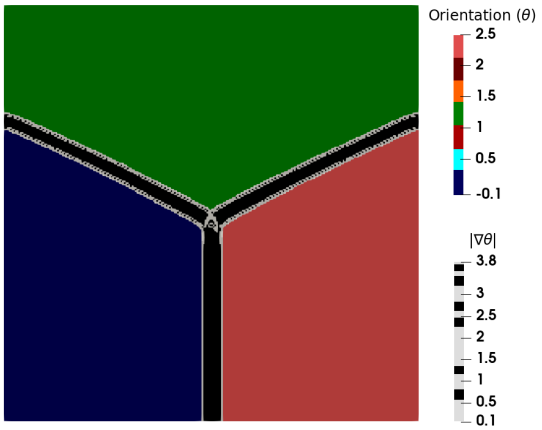

(c)

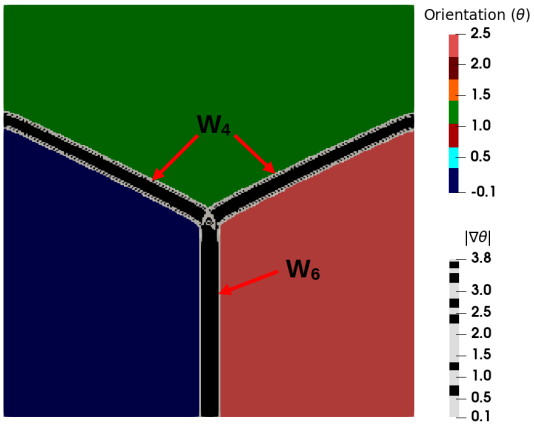

(d)

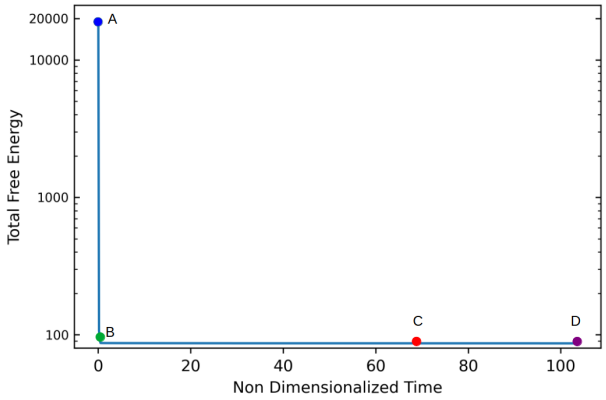

(e)

Figure 6: The temporal evolution of orientation ($\theta = 0,\ 1.2,\ \&\ 2.4$) in a tri-crystal with sharp curved GBs initial condition at time (a) $t = 0$, (b) $t = 0.31$, (c) 68.60, and (d) $t = 103.49$. The energy density function is SED and $\alpha = 0.07$. The system achieves the final equilibrium profile corresponding to $max_{xx}|(\theta^{t+dt} - \theta^t)/dt| < 1 \times 10^{-3}$. The corresponding total energy evolution over time is shown in (e), where points A, B, C, and D indicate the total energy of the system at the states depicted in (a), (b), (c), and (d), respectively. Different colors represent different orientations of the grains, and black color represents GBs corresponding to energy density wells in Fig. 2.

Finally, the objective is to demonstrate the model's ability to satisfy the Herring condition [33, 34] by achieving local equilibrium at the triple junction through the force balance of the GBs. It is assumed that the torque term is negligible for general boundaries located far away from the special boundaries [66], such as Coincident Site Lattice (CSL) boundaries like $\Sigma 3$ and $\Sigma 5$. These CSL boundaries typically exhibit lower GB energy compared to typical HAGBs [61].

While the results depicted in Fig. 5b and Fig. 6d also exhibit compliance with the Herring condition, it is important to note that their initial conditions might be in close proximity to the final equilibrium profile achieved by the model due to the Herring condition. This proximity could introduce a degree of bias in the initial conditions. To mitigate this potential bias, an initial condition significantly distant from the final equilibrium profile has been deliberately selected, as depicted in Fig. 7a. As time progresses, the system undergoes evolution at the triple junction, consistently yielding dihedral angles close to 120° between the GBs. This stable configuration is maintained throughout the evolution, as illustrated in Fig. 7b and Fig. 7c. In Fig. 7d, the system extends the GB evolution to the simulation domain boundaries, revealing the triple junction with dihedral angles close to 120° between the GBs as a notably favorable energy configuration. These simulation results showcase the model's capability to fulfill the Herring condition, even when starting from an unbiased initial condition.

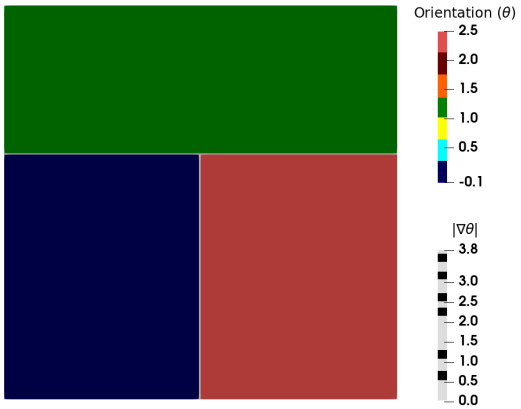

(a)

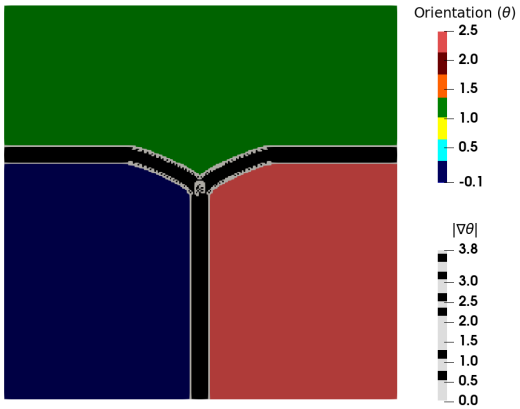

(b)

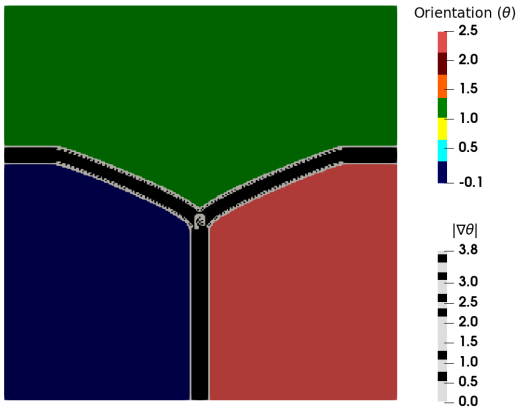

(c)

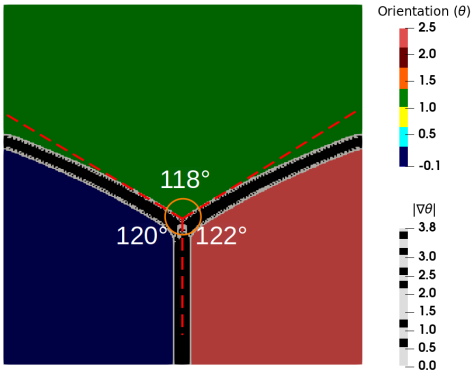

(d)

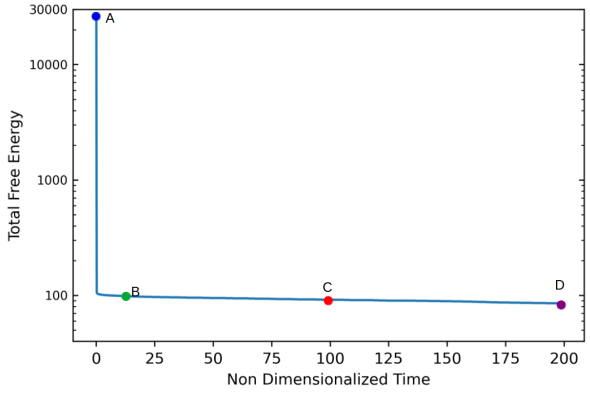

(e)

Figure 7: The temporal evolution of orientation ($\theta = 0,\ 1.2,\ \&\ 2.4$) in a tri-crystal with flat GBs initial condition at time (a) $t = 0$, (b) $t = 11.63$, (c) 95.09, and (d) $t = 198.65$. The energy density function is SED and $\alpha = 0.09$. The corresponding total energy evolution over time is shown in (e), where points A, B, C, and D indicate the total energy of the system at the states depicted in (a), (b), (c), and (d), respectively. Different colours represent different orientations of the grains, and black colour represents GBs corresponding to energy density wells in Fig. 2.

5. Conclusions

The present study leads to the following conclusions:

- The current study is the extension of our 1-D model [1] where an experimentally measured grain boundary (GB) energy function is used to drive the evolution of GBs in 2-D and addresses rotational invariance within the model.
- The SED (ϕ_s) has been chosen for use in this study as it effectively captures all the troughs in the experimental data and is assumed to represent the ground truth [1].
- A Finite Element Method (FEM) approach is applied to solve the gradient flow equation, providing a computational framework that naturally accommodates jump conditions. This is in contrast with the Finite Difference Method (FDM) approach utilized in our previous study [1] where special care had to be taken to impose the crucial jump condition at kinks.
- The model captures equilibrium transition layers in a 2-D grain array, serving as an idealized representation of equilibrium HAGBs,
- The present model incorporates aspects of idealized grain rotation, curvature-driven GB motion, and grain growth in 2-D,
- The model attains local equilibrium at the triple junction by adhering to the Herring condition.

The present isotropic model successfully captures idealized features such as equilibrium HAGBs, grain rotation, curvature-driven GB motion, grain growth, and triple junctions that satisfy the Herring condition in our 2-D simulations. Incorporating GB inclination dependency into the existing model and application of this GB model in a Crystal Plasticity (CP) framework is a natural extension, allowing for an in-depth exploration of the impact of anisotropy and deformation on microstructural evolution. Challenges lie ahead for our experimentally informed setup, particularly in addressing the computational demands associated with three-dimensional (3-D) simulations, mathematical complexities associated with the anisotropic model, and the comprehensive representation of coupled interfacial–bulk mechanics of defects, as elaborated in Section 1 of [1]. These endeavours aim to accurately model the GB evolution and the mechanics of GB junctions, with the hope of understanding the design of the microstructure of the material to serve the needs of diverse applications.

Acknowledgment

The work of AA is supported by the NSF grant NSF OIA-DMR #2021019. ALR acknowledges the financial support provided by IIT Bombay for Ph.D. student SA. ALR also acknowledges the partial financial support from Aeronautics Research Development Board (ARDB) vide Grant #GTMAP1952 for part of a Computational Facility that was used for this work. SA would like to thank Dr. M Dinachandra, IPDF, IIT Bombay for his valuable insights and assistance in debugging the source code.

Conflict of Interest

The authors have no relevant financial or non-financial interests to disclose.

References

[1] S Syed Ansari, Amit Acharya, and Alankar Alankar. An experimentally informed continuum grain boundary model. Mathematics and Mechanics of Solids, 0(0):10812865231223921, 0. doi: 10.1177/10812865231223921. URL https://doi.org/10.1177/10812865231223921.

[2] A.P. Sutton and R.W. Balluffi. Interfaces in Crystalline Materials. Oxford Classic Texts in the Physical Sciences. OUP Oxford, 2006. ISBN 9780199211067.

[3] Ryo Kobayashi, James A. Warren, and W. Craig Carter. A continuum model of grain boundaries. Physica D: Nonlinear Phenomena, 140(1-2):141–150, 2000.

[4] Luchan Zhang, Jian Han, David J. Srolovitz, and Yang Xiang. Equation of motion for grain boundaries in polycrystals. npj Computational Materials, 7(1):1–8, 2021.

[5] Kongtao Chen, Jian Han, and David J. Srolovitz. On the temperature dependence of grain boundary mobility. Acta Materialia, 194:412–421, 2020.

[6] Chaozhen Wei, Spencer L. Thomas, Jian Han, David J. Srolovitz, and Yang Xiang. A continuum multi-disconnection-mode model for grain boundary migration. Journal of the Mechanics and Physics of Solids, 133:103731, 2019.

[7] A.D. Rollett, D.J. Srolovitz, and M.P. Anderson. Simulation and theory of abnormal grain growth—anisotropic grain boundary energies and mobilities. Acta Metallurgica, 37(4):1227–1240, 1989. ISSN 0001-6160. doi: https://doi.org/10.1016/0001-6160(89)90117-X. URL https://www.sciencedirect.com/science/article/pii/000161608990117X.

[8] Rajchawit Sarochawikasit, Cong Wang, Poom Kumam, Hossein Beladi, Taira Okita, Gregory S. Rohrer, and Sutatch Ratanaphan. Grain boundary energy function for α iron. Materialia, 19:101186, 2021. ISSN 2589-1529. doi: https://doi.org/10.1016/j.mtla.2021.101186. URL https://www.sciencedirect.com/science/article/pii/S2589152921001897.

[9] Sutatch Ratanaphan, Rajchawit Sarochawikasit, Noppadol Kumanuvong, Sho Hayakawa, Hossein Beladi, Gregory S. Rohrer, and Taira Okita. Atomistic simulations of grain boundary energies in austenitic steel. Journal of Materials Science, 54(7):5570–5583, Apr 2019. ISSN 1573-4803. doi: 10.1007/s10853-018-03297-4. URL https://doi.org/10.1007/s10853-018-03297-4.

[10] John W. Cahn and John E. Hilliard. Free energy of a nonuniform system. I. Interfacial free energy. The Journal of Chemical Physics, 28(2):258–267, 1958.

[11] Gabriel Martine La Boissonière, Rustum Choksi, Katayun Barmak, and Selim Esedoğlu. Statistics of grain growth: Experiment versus the phase-field-crystal and Mullins models. Materialia, 6:100280, 2019. ISSN 2589-1529. doi: https://doi.org/10.1016/j.mtla.2019.100280. URL https://www.sciencedirect.com/science/article/pii/S2589152919300766.

[12] Selim Esedoğlu. Grain size distribution under simultaneous grain boundary migration and grain rotation in two dimensions. Computational Materials Science, 121:209–216, 2016. ISSN 0927-0256. doi: https://doi.org/10.1016/j.commatsci.2016.04.022. URL https://www.sciencedirect.com/science/article/pii/S0927025616301811.

[13] C. Truesdell and W. Noll. The Non-Linear Field Theories of Mechanics, pages 1–579. Springer Berlin Heidelberg, Berlin, Heidelberg, 2004. ISBN 978-3-662-10388-3. doi: 10.1007/978-3-662-10388-3_1. URL https://doi.org/10.1007/978-3-662-10388-3_1.

[14] Patricio Aviles and Yoshikazu Giga. The distance function and defect energy. Proceedings of the Royal Society of Edinburgh Section A: Mathematics, 126(5):923–938, 1996.

[15] M.C. Cross and Alan C. Newell. Convection patterns in large aspect ratio systems. Physica D: Nonlinear Phenomena, 10(3):299–328, 1984.

[16] K.B. Glasner. Grain boundary motion arising from the gradient flow of the Aviles–Giga functional. Physica D: Nonlinear Phenomena, 215(1):80–98, 2006.

[17] Robert V. Kohn and Stefan Müller. Surface energy and microstructure in coherent phase transitions. Communications on Pure and Applied Mathematics, 47(4):405–435, 1994.
[18] Nikhil Chandra Admal, Javier Segurado, and Jaime Marian. A three-dimensional misorientation axis- and inclination-dependent Kobayashi–Warren–Carter grain boundary model. Journal of the Mechanics and Physics of Solids, 128:32–53, 2019.
[19] James A Warren, W Craig Carter, and Ryo Kobayashi. A phase field model of the impingement of solidifying particles. Physica A: Statistical Mechanics and its Applications, 261(1-2):159–166, 1998.
[20] Alexander E. Lobkovsky and James A. Warren. Sharp interface limit of a phase-field model of crystal grains. Phys. Rev. E, 63:051605, Apr 2001. doi: 10.1103/PhysRevE.63.051605. URL https://link.aps.org/doi/10.1103/PhysRevE.63.051605.
[21] Nikolas Provatas and Ken Elder. Phase-Field Methods in Materials Science and Engineering, chapter 1, pages 1–7. John Wiley & Sons, Ltd, 2010. ISBN 9783527631520. doi: https://doi.org/10.1002/9783527631520.ch1. URL https://onlinelibrary.wiley.com/doi/abs/10.1002/9783527631520.ch1.
[22] R. S. Qin and H. K. Bhadeshia. Phase field method. Materials Science and Technology, 26(7):803–811, 2010. doi: 10.1179/174328409X453190. URL https://doi.org/10.1179/174328409X453190.
[23] Long-Qing Chen. Phase-Field Models for Microstructure Evolution. Annual Review of Materials Research, 32(1):113–140, 2002. doi: 10.1146/annurev.matsci.32.112001.132041. URL https://doi.org/10.1146/annurev.matsci.32.112001.132041.
[24] Nele Moelans, Bart Blanpain, and Patrick Wollants. An introduction to phase-field modeling of microstructure evolution. Calphad, 32(2):268–294, 2008. ISSN 0364-5916. doi: https://doi.org/10.1016/j.calphad.2007.11.003. URL https://www.sciencedirect.com/science/article/pii/S0364591607000880.
[25] Damien Tourret, Hong Liu, and Javier LLorca. Phase-field modeling of microstructure evolution: Recent applications, perspectives and challenges. Progress in Materials Science, 123:100810, 2022. ISSN 0079-6425. doi: https://doi.org/10.1016/j.pmatsci.2021.100810. URL https://www.sciencedirect.com/science/article/pii/S0079642521000347. A Festschrift in Honor of Brian Cantor.
[26] Samuel M. Allen and John W. Cahn. A microscopic theory for antiphase boundary motion and its application to antiphase domain coarsening. Acta Metallurgica, 27(6):1085–1095, 1979.
[27] D. Fan and L.-Q. Chen. Computer simulation of grain growth using a continuum field model. Acta Materialia, 45(2):611–622, 1997. ISSN 1359-6454. doi: https://doi.org/10.1016/S1359-6454(96)00200-5. URL https://www.sciencedirect.com/science/article/pii/S1359645496002005.
[28] C.E. Krill III and L.-Q. Chen. Computer simulation of 3-D grain growth using a phase-field model. Acta Materialia, 50(12):3059–3075, 2002. ISSN 1359-6454. doi: https://doi.org/10.1016/S1359-6454(02)00084-8. URL https://www.sciencedirect.com/science/article/pii/S1359645402000848.
[29] Jin Zhang, Wolfgang Ludwig, Yubin Zhang, Hans Henrik B. Sørensen, David J. Rowenhorst, Akinori Yamanaka, Peter W. Voorhees, and Henning F. Poulsen. Grain boundary mobilities in polycrystals. Acta Materialia, 191:211–220, 2020. ISSN 1359-6454. doi: https://doi.org/10.1016/j.actamat.2020.03.044. URL https://www.sciencedirect.com/science/article/pii/S1359645420302317.
[30] I.M. McKenna, S.O. Poulsen, E.M. Lauridsen, W. Ludwig, and P.W. Voorhees. Grain growth in four dimensions: A comparison between simulation and experiment. Acta Materialia, 78:125–134, 2014. ISSN 1359-6454. doi: https://doi.org/10.1016/j.actamat.2014.06.028. URL https://www.sciencedirect.com/science/article/pii/S1359645414004480.
[31] David Kinderlehrer, Irene Livshits, and Shlomo Ta'asan. A variational approach to modeling and simulation of grain growth. SIAM Journal on Scientific Computing, 28(5):1694–1715, 2006. doi: 10.1137/030601971. URL https://doi.org/10.1137/030601971.
[32] W. W. Mullins. Two-dimensional motion of idealized grain boundaries. Journal of Applied Physics, 27(8):900–904, 1956. doi: 10.1063/1.1722511. URL https://doi.org/10.1063/1.1722511.
[33] Conyers Herring and W.E. Kingston. The Physics of Powder Metallurgy. WE Kingston, Edition: McGraw Hill, New York, 1951.
[34] Conyers Herring. The Use of Classical Macroscopic Concepts in Surface Energy Problems. In Robert

Gomer and Cyril Stanley Smith, editors, Structure and Properties of Solid Surfaces, page 5, January 1953.

[35] Matt Elsey, Selim Esedoḡlu, and Peter Smereka. Diffusion generated motion for grain growth in two and three dimensions. Journal of Computational Physics, 228(21):8015–8033, 2009. ISSN 0021-9991. doi: https://doi.org/10.1016/j.jcp.2009.07.020. URL https://www.sciencedirect.com/science/article/pii/S0021999109004082.

[36] Selim Esedoḡlu, Steven Ruuth, and Richard Tsai. Diffusion generated motion using signed distance functions. Journal of Computational Physics, 229(4):1017–1042, 2010. ISSN 0021-9991. doi: https://doi.org/10.1016/j.jcp.2009.10.002. URL https://www.sciencedirect.com/science/article/pii/S0021999109005476.

[37] Håkan Hallberg and Vasily V Bulatov. Modeling of grain growth under fully anisotropic grain boundary energy. Modelling and Simulation in Materials Science and Engineering, 27(4):045002, apr 2019. doi: 10.1088/1361-651X/ab0c6c. URL https://dx.doi.org/10.1088/1361-651X/ab0c6c.

[38] José D. Niño and Oliver K. Johnson. Influence of grain boundary energy anisotropy on the evolution of grain boundary network structure during 3d anisotropic grain growth. Computational Materials Science, 217:111879, 2023. ISSN 0927-0256. doi: https://doi.org/10.1016/j.commatsci.2022.111879. URL https://www.sciencedirect.com/science/article/pii/S0927025622005900.

[39] Nikhil Chandra Admal, Giacomo Po, and Jaime Marian. A unified framework for polycrystal plasticity with grain boundary evolution. International Journal of Plasticity, 106:1–30, 2018.

[40] Anup Basak and Anurag Gupta. A two-dimensional study of coupled grain boundary motion using the level set method. Modelling and Simulation in Materials Science and Engineering, 22(5):055022, jun 2014. doi: 10.1088/0965-0393/22/5/055022. URL https://doi.org/10.1088/0965-0393/22/5/055022.

[41] Anup Basak and Anurag Gupta. A three-dimensional study of coupled grain boundary motion with junctions. Proceedings of the Royal Society A: Mathematical, Physical and Engineering Sciences, 471 (2178):20150127, 2015.

[42] Morton E. Gurtin and Michel E. Jabbour. Interface evolution in three dimensions with curvature-dependent energy and surface diffusion:interface-controlled evolution, phase transitions, epitaxial growth of elastic films. Archive for Rational Mechanics and Analysis, 163(3):171–208, 2002. doi: 10.1007/s002050200193. URL https://doi.org/10.1007/s002050200193.

[43] A.D. Rollett, C.C. Yang, W.W. Mullins, B.L. Adams, C.T. Wu, D. Kinderlehrer, S. Ta'asan, F. Manolache, C. Liu, I. Livshits, et al. Grain boundary property determination through measurement of triple junction geometry and crystallography. In Int. Conf. on Grain Growth and Recrystallization, Aachen, Germany, pages 165–176, 2001.

[44] Aditi Bhattacharya, Yu-Feng Shen, Christopher M. Hefferan, Shiu Fai Li, Jonathan Lind, Robert M. Suter, Carl E. Krill, and Gregory S. Rohrer. Grain boundary velocity and curvature are not correlated in Ni polycrystals. Science, 374(6564):189–193, 2021. doi: 10.1126/science.abj3210. URL https://www.science.org/doi/abs/10.1126/science.abj3210.

[45] Luchan Zhang, Jian Han, Yang Xiang, and David J. Srolovitz. Equation of motion for a grain boundary. Phys. Rev. Lett., 119:246101, Dec 2017. doi: 10.1103/PhysRevLett.119.246101. URL https://link.aps.org/doi/10.1103/PhysRevLett.119.246101.

[46] Jian Han, David J. Srolovitz, and Marco Salvalaglio. Disconnection-mediated migration of interfaces in microstructures: I. continuum model. Acta Materialia, page 117178, 2021. ISSN 1359-6454. doi: https://doi.org/10.1016/j.actamat.2021.117178. URL https://www.sciencedirect.com/science/article/pii/S1359645421005589.

[47] Marco Salvalaglio, David J. Srolovitz, and Jian Han. Disconnection-mediated migration of interfaces in microstructures: Ii. diffuse interface simulations. Acta Materialia, 227:117463, 2022. ISSN 1359-6454. doi: https://doi.org/10.1016/j.actamat.2021.117463. URL https://www.sciencedirect.com/science/article/pii/S1359645421008429.

[48] G.C. Hasson and C. Goux. Interfacial energies of tilt boundaries in aluminium. Experimental and theoretical determination. Scripta Metallurgica, 5(10):889–894, 1971.

[49] H. Miura, M. Kato, and T. Mori. Determination of boundary energies of Cu from the shape of boundary SiO2 particles. Le Journal de Physique Colloques, 51(C1):C1–263, 1990.

[50] Jia Li, Shen J. Dillon, and Gregory S. Rohrer. Relative grain boundary area and energy distributions in nickel. Acta Materialia, 57(14):4304–4311, 2009. ISSN 1359-6454. doi: https://doi.org/10.1016/j.actamat.2009.06.004. URL https://www.sciencedirect.com/science/article/pii/S1359645409003425.

[51] W. T. Read and W. Shockley. Dislocation Models of Crystal Grain Boundaries. Phys. Rev., 78:275–289, May 1950. doi: 10.1103/PhysRev.78.275. URL https://link.aps.org/doi/10.1103/PhysRev.78.275.

[52] Vasily V. Bulatov, Bryan W. Reed, and Mukul Kumar. Grain boundary energy function for fcc metals. Acta Materialia, 65:161–175, 2014. ISSN 1359-6454. doi: https://doi.org/10.1016/j.actamat.2013.10.057. URL https://www.sciencedirect.com/science/article/pii/S1359645413008203.

[53] Naoki Takata, Kenichi Ikeda, Fusahito Yoshida, H. Nakashima, and Hiroshi Abe. Grain boundary structure and its energy of< 110> symmetric tilt boundary in copper. In Materials Science Forum, volume 467, pages 807–812. Trans Tech Publ, 2004.

[54] Daniel Arndt, Wolfgang Bangerth, Bruno Blais, Marc Fehling, Rene Gassmöller, Timo Heister, Luca Heltai, Uwe Köcher, Martin Kronbichler, Matthias Maier, Peter Munch, Jean-Paul Pelteret, Sebastian Proell, Konrad Simon, Bruno Turcksin, David Wells, and Jiaqi Zhang. The `deal.II` library, version 9.3. Journal of Numerical Mathematics, 29(3):171–186, 2021. doi: 10.1515/jnma-2021-0081. URL https://dealii.org/deal93-preprint.pdf.

[55] R Kobayashi and Y Giga. Equations with singular diffusivity. Journal of Statistical Physics, 95(5):1187–1220, June 1999.

[56] Eugene Isaacson and Herbert Bishop Keller. Analysis of Numerical Methods. Dover Publications, 1994.

[57] G. Gottstein, D.A. Molodov, L.S. Shvindlerman, D.J. Srolovitz, and M. Winning. Grain boundary migration: misorientation dependence. Current Opinion in Solid State and Materials Science, 5(1):9–14, 2001. ISSN 1359-0286. doi: https://doi.org/10.1016/S1359-0286(00)00030-9. URL https://www.sciencedirect.com/science/article/pii/S1359028600000309.

[58] Dmitri A. Molodov. Motion of Grain Boundaries: Experiments on Bicrystals. Diffusion Foundations, 5:247–271, 8 2015. doi: 10.4028/www.scientific.net/DF.5.247.

[59] D.M. Kirch, B. Zhao, D.A. Molodov, and G. Gottstein. Faceting of low-angle <100> tilt grain boundaries in aluminum. Scripta Materialia, 56(11):939–942, 2007. ISSN 1359-6462. doi: https://doi.org/10.1016/j.scriptamat.2007.02.010. URL https://www.sciencedirect.com/science/article/pii/S1359646207001376.

[60] D.M. Kirch, E. Jannot, L.A. Barrales-Mora, D.A. Molodov, and G. Gottstein. Inclination dependence of grain boundary energy and its impact on the faceting and kinetics of tilt grain boundaries in aluminum. Acta Materialia, 56(18):4998–5011, 2008. ISSN 1359-6454. doi: https://doi.org/10.1016/j.actamat.2008.06.017. URL https://www.sciencedirect.com/science/article/pii/S1359645408004497.

[61] F.J. Humphreys and M. Hatherly. Recrystallization and Related Annealing Phenomena (Second Edition). pages 91–119. Elsevier, Oxford, Second edition, 2004. ISBN 978-0-08-044164-1. doi: https://doi.org/10.1016/B978-008044164-1/50008-6. URL https://www.sciencedirect.com/science/article/pii/B9780080441641500086.

[62] K.E. Harris, V.V. Singh, and A.H. King. Grain rotation in thin films of gold. Acta Materialia, 46(8):2623–2633, 1998. ISSN 1359-6454. doi: https://doi.org/10.1016/S1359-6454(97)00467-9. URL https://www.sciencedirect.com/science/article/pii/S1359645497004679.

[63] Hsun Hu. Direct observations on the annealing of a si-fe crystal in the electron microscope. Transactions of the Metallurgical Society of AIME, 224(1):75–84, 1962.

[64] M. Upmanyu, D.J. Srolovitz, A.E. Lobkovsky, J.A. Warren, and W.C. Carter. Simultaneous grain boundary migration and grain rotation. Acta Materialia, 54(7):1707–1719, 2006. ISSN 1359-6454. doi: https://doi.org/10.1016/j.actamat.2005.11.036. URL https://www.sciencedirect.com/science/article/pii/S135964540500707X.

[65] A.J Haslam, S.R Phillpot, D Wolf, D Moldovan, and H Gleiter. Mechanisms of grain growth in

nanocrystalline fcc metals by molecular-dynamics simulation. Materials Science and Engineering: A, 318(1):293–312, 2001. ISSN 0921-5093. doi: https://doi.org/10.1016/S0921-5093(01)01266-7. URL https://www.sciencedirect.com/science/article/pii/S0921509301012667.

[66] G Gottstein and LS Shvindlerman. Grain boundary migration in metals: Thermodynamics, kinetics, applications. In Grain Boundary Migration in Metals: Thermodynamics, Kinetics, Applications, Second Edition, pages 1–701. 2009.